DISCLAIMER

LBNL-49347

Ammonia Conversion and NO_x Formation in Laminar Coflowing Nonpremixed Methane-Air Flames

Neal Sullivan
ITN Energy Systems
8130 Shaffer Parkway
Littleton, Colorado 80127 USA

Anker Jensen, Peter Glarborg
Department of Chemical Engineering
Technical University of Denmark
DK-2800, Lyngby, Denmark

Marcus S. Day, Joseph F. Grcar, John B. Bell
Center for Computational Sciences and Engineering
Lawrence Berkeley National Laboratory
Berkeley, California 94720 USA

Christopher J. Pope
Combustion Research Facility
Sandia National Laboratories
Livermore, California 94551 USA

Robert J. Kee
Engineering Division
Colorado School of Mines
Golden, Colorado 80401 USA

This work was supported under the Applied Mathematical Sciences Program by the Director, Office of Science, Office of Advanced Scientific Computing Research, Mathematical, Information, and Computational Sciences Division of the U.S. Department of Energy, contract No. DE-AC03-76SF00098.

Ammonia Conversion and NO_x Formation in Laminar Coflowing Nonpremixed Methane-Air Flames

Abstract

This paper reports on a combined experimental and modeling investigation of NO_x formation in nitrogen-diluted laminar methane diffusion flames seeded with ammonia. The methane-ammonia mixture is a surrogate for biomass fuels which contain significant fuel-bound nitrogen. The experiments use flue-gas sampling to measure the concentration of stable species in the exhaust gas, including NO, O_2, CO, and CO_2. The computations evolve a two-dimensional low Mach number model using a solution-adaptive projection algorithm to capture fine-scale features of the flame. The model includes detailed thermodynamics and chemical kinetics, differential diffusion, buoyancy, and radiative losses. The models shows good agreement with the measurements over the full range of experimental NH_3 seeding amounts. As more NH_3 is added, a greater percentage is converted to N_2 rather than to NO. The simulation results are further analyzed to trace the changes in NO formation mechanisms with increasing amounts of ammonia in the fuel.

1 Introduction

The dependence on combustion for meeting world energy demands has given rise to many harmful side effects, such as photochemical smog and "acid rain," due in part to the emissions of the nitrogen oxides NO and NO_2, collectively termed NO_x. With increasing governmental regulation of pollutant emission, the control and reduction of NO_x is not only an environmental matter, but a financial one as well [1]. The problem is exacerbated by a desire to use a combination of national coal reserves and/or biomass power supplies to alleviate oil dependence. Coal and biomass fuels typically contain large amounts of chemically bound nitrogen — as much as 2% by mass. The nitrogenous gases that vaporize from these solid fuels during pyrolysis are converted in the flame to either N_2 or NO_x, depending on the local combustion conditions.

Though the chemical form taken by vaporized fuel-nitrogen has little influence on the overall conversion rate to NO [2–6], the nitrogen-containing compounds typically form either HCN or NH_3. The fraction of each species formed remains the subject of ongoing research [7, 8]; however, in volatiles from biomass feedstocks, the ammonia concentration is orders of magnitude higher than those of other fuel-nitrogen species [9]. Thus, we use an ammonia-seeded fuel for the present study.

The main chemical formation routes of NO_x in a combustion reaction are well established. At temperatures exceeding 1800 K, atmospheric nitrogen is oxidized to NO [2] through the thermal (or Zeldovich) mechanism. In the prompt (or Fenimore)

mechanism, NO is formed in the flame zone through reactions between molecular nitrogen and hydrocarbon radicals [10]. In the fuel-nitrogen mechanisms (shown in Fig. 1, adapted from Miller and Bowman [11]), nitrogenous species that vaporize from the solid fuel undergo hydrogen abstraction reactions. Each resulting NH_i radical can then participate in one of two subsequent reaction mechanisms: 1) oxidation leading to NO formation; or 2) conversion to molecular nitrogen through reactions that additionally consume NO [12].

Many previous studies of NO_x formation have focused on the relative roles of thermal and prompt formation routes under a variety of conditions [13–16]. However, NO_x formed from the combustion of biomass and other solid fuels will be heavily dominated by the conversion of large amounts of fuel-bound nitrogen; thermal and prompt mechanisms will be comparatively insignificant. In spite of its importance, fuel-nitrogen NO_x formation has seen comparatively little investigation.

Like most solid fuels, vapors from biomass are burned in nonpremixed flames. For this reason we consider an axisymmetric laminar coflowing nonpremixed flame, schematically depicted in Fig. 2. This represents a reasonably complete model system for studying NO_x formation during the combustion of vaporized biomass volatiles. The configuration affords evaluation of the NO_x-production pathways in a realistic flow field, without introducing models for fluid turbulence or compromising the fidelity of the chemical kinetics representation. In this configuration, fuel issues from a nozzle of radius r_f and wall thickness δ, while oxidizer flows from a co-annular tube of radius r_{ox}. The two streams are mixed through entrainment and diffusion, and for suitable fuel and oxidizer flow rates, a stable flame is produced. The model system is assumed to be invariant in the azimuthal coordinate, reducing the problem to two spatial dimensions: axial z and radial r.

A nonpremixed flame forms as a complex balance of chemical reactions and species transport through advection and diffusion. Early models of this complex system assumed negligible axial diffusion (ie., the "boundary layer" assumption). Burke and Schumann [17] demonstrated that such a model could accurately predict diffusion flame heights. More complex analyses by Roper [18, 19] and Gordon [20, 21] generalized the approach into a well-established computational flame analysis tool. Miller and Kee [22] combined the boundary layer assumption with detailed reaction kinetics to simulate a hydrogen-air laminar nonpremixed flame. Interestingly, they found that flame-zone radical concentrations may exceed equilibrium values by more than an order of magnitude. Super-equilibrium atomic O concentrations may strongly affect NO_x formation [2, 13].

For lower-speed flows, where axial diffusion becomes comparable to advective transport processes, Chung and Law [23] demonstrated that the boundary layer assumption leads to poor predictions for flame height and shape. The experimental work of Ishizuka and Sakai [24] and in numerical studies by Takagi and Xu [25] indicated that axial diffusion effects played a key role in the gross diffusion flame structure.

The work of Smooke *et al.* [26, 27] was apparently the first to successfully model the coflowing laminar nonpremixed flame without making use of the boundary layer approximation. The two-dimensional model has served well as a tool to provide significant insight into the structure of diffusion flames [26–31], including NO formation [14]. However, no study of fuel-nitrogen effects has yet been performed.

Nishioka *et al.* [32] correlated flame structure from simulations of axisymmetric, coflowing, nonpremixed flames with that of one-dimensional opposed-flow nonpremixed flames through a "representative diffusion time." The ability to capture the physics of this two-dimensional problem through a series of one-dimensional calculations represents a significant breakthrough and decrease in complexity. However, in a subsequent study, Zhu *et al.* [33] found that this correlation breaks down when considering NO_x formation, indicating that emission characteristics from 2-D flames are different from those of 1-D flames.

In this study, we investigate an ammonia-enriched laminar nonpremixed methane-air flame through both experiment and computation. The focus of the work is to understand how the fuel-nitrogen routes for NO formation differ from those of flames without fuel-nitrogen. The computational model incorporates a number of detailed chemical mechanisms, as well as buoyancy effects, differential diffusion and an optically thin radiation model. The simulations provide steady, axisymmetric spatially-resolved species and thermal profiles for detailed analysis of the NO production pathways. Experimental data is used to validate global predictions of the model, and to provide a basis for comparing discrepancies between different detailed chemistry mechanisms.

2 Experimental Setup

The coflowing laminar nonpremixed flame shown in Fig. 2 is established in a quartz reactor of dimensions $r_f = 6$ mm, $r_{ox} = 14$ mm, $\delta = 1$ mm, and height $h = 760$ mm. Long entrance lengths are provided for the inlet gases so that fully developed flow is established in the fuel and oxidizer tubes upstream of the fuel nozzle. The fuel is a mixture of methane and nitrogen at flow rates of 150 mL/min and 220 mL/min, respectively. Ammonia is added to the fuel stream to establish an initial fuel-nitrogen mole fraction ranging from 0 to 1000 ppm averaged over the total fuel-oxidizer mixture. The oxidizer is a mixture of research grade oxygen and nitrogen at flow rates of 840 mL/min and 3160 mL/min, respectively (21% oxygen). The nitrogen dilution in the fuel stream results in a relatively cool flame, where peak temperatures rise only slightly above the 1800K required for significant thermal NO production. Flue gases from the reactor are dehumidified through a water trap upstream of Hartmann & Braun gas analyzers for measurement of O_2, NO, CO_2 and CO concentration.

The computational domain begins ($z = 0$) at the exit edge of the fuel tube and extends downstream 11 cm. This domain is shorter than the 76 cm quartz reactor, but it is much longer than the flame as indicated by peak temperature. Inflow boundary conditions specify fully-developed laminar pipe flow for the co-annular fuel and oxidizer regions ($\mathrm{Re}_{\mathrm{fuel}} = 41$, $\mathrm{Re}_{\mathrm{ox}} = 127$). No-slip conditions apply along the outer wall and fuel tube edge, and a non-reflecting outflow boundary is enforced at $z = 11$ cm. The outer wall of the domain has a fixed piecewise-linear temperature profile obtained by experimental measurement (rising from 500 K at the inlet to 800 K at 6 cm, then dropping to 300 K at 50 cm); the fuel tube edge adjacent to the inflow boundary is assumed to be adiabatic. All inlet gases enter the system at standard temperature and pressure.

3 The Computational Model

We use the adaptive axisymmetric two-dimensional computational approach presented by Day and Bell [34] for low Mach number flows. In the low Mach number limit, the equations describing momentum transport and conservation of species and enthalpy are given by:

$$\rho \frac{D\vec{v}}{Dt} = \nabla\pi + \nabla \cdot \tau + \rho\vec{g} \tag{1}$$

$$\frac{\partial \rho Y_k}{\partial t} + \nabla \cdot \vec{v}\rho Y_k = \nabla \cdot \rho D_k \nabla Y_k + M_k \dot{\omega}_k \tag{2}$$

$$\frac{\partial \rho h}{\partial t} + \nabla \cdot \vec{v}\rho h = \nabla \cdot \lambda \nabla T + \sum_{k=1}^{K} \nabla \cdot \rho h_k D_k \nabla Y_k + Q \tag{3}$$

where ρ is the density, $\vec{v}$ is the velocity, $\vec{g}$ is the gravity vector, h is the enthalpy of the gas mixture, and T is the temperature. For species $k = 1, \ldots, K$, Y_k is the mass fraction, M_k is the molar mass, and $\dot{\omega}_k$ is the molar production rate due to chemical reaction, which is specified via a collection of elementary reactions using a CHEMKIN [35] compatible database. Q is the heat source from radiation calculated from an optically thin (emission only) model:

$$Q(T, Y_k) = 4\sigma \sum_{k=1}^{K} Y_k M_k p \, a_{P,k} (T^4 - T_b^4)$$

where σ is the Stefan-Boltzmann constant, $a_{P,k}$ is the Planck mean absorption coefficient for species k, and T_b is the background temperature [36]. The stress tensor is given by:

$$\tau = \mu \left(\frac{\partial \vec{v}_i}{\partial \vec{v}_j} + \frac{\partial \vec{v}_j}{\partial x_i} - \frac{2}{3} \delta_{i,j} \nabla \cdot \vec{v} \right)$$

where $\mu(Y_1, \ldots, Y_K, T)$ is the viscosity, λ is the mixture-averaged thermal conductivity, and for species k, D_k is the species mixture-averaged diffusion coefficient [37], and $h_k(T)$ is the enthalpy.

These time-dependent equations are supplemented by an equation of state:

$$p_0 = \rho RT \sum_{k=1}^{K} \frac{Y_k}{M_k} \tag{4}$$

and by a relationship between enthalpy, species and temperature:

$$h = \sum_{k=1}^{K} Y_k h_k(T) \; . \tag{5}$$

The evolution specified by Eqs. 1–3 is subject to the constraint on the velocity:

$$\begin{aligned} \nabla \cdot \vec{v} \;\; = \;\; & \frac{1}{\rho C_p T} \left(\nabla \cdot \lambda \nabla T + Q + \sum_{k=1}^{K} \rho D_k \nabla Y_k \cdot \nabla h_k \right) \\ & + \frac{1}{\rho} \sum_{k=1}^{K} \frac{W}{M_k} \nabla \cdot \rho D_k \nabla Y_k + \frac{1}{\rho} \sum_{k=1}^{K} \left(\frac{W}{M_k} - \frac{h_k}{C_p T} \right) \dot{\omega}_k \end{aligned} \tag{6}$$

where $W = \left(\sum_{k=1}^{K} Y_k / M_k \right)^{-1}$ and $C_p = \left(\sum_{k=1}^{K} Y_k (dh_k/dT) \right)^{-1}$. The constraint in Eq. 6 is obtained by differentiating the equation of state in the frame of the moving fluid and replacing the Lagrangian derivatives by expressions obtained from Eqs. 2, 3, and 5.

The discretization methodology is based on a robust projection formulation that accommodates large density contrasts. The algorithm uses an operator-split treatment of stiff reaction terms and includes effects of differential diffusion in both spatial coordinates. The basic computational approach is embedded in an adaptive projection framework that uses structured hierarchical grids with subcycling in time that preserves the discrete conservation properties of the underlying single-grid algorithm. The flow is "ignited" at time $t = 0$ and allowed to evolve until steady-state conditions are achieved (convergence is monitored by the axial profile of the radially integrated NO profile). Details of the discretization and implementation are discussed in Day and Bell [34].

The simulations are performed using two different chemical mechanisms for combustion. The first is a mechanism proposed by Glarborg *et al.* consisting of 66 species and 447 reactions [38]. It contains the oxidation of C_1 and C_2 hydrocarbons, HCN, and NH_3 with a subset describing interactions between hydrocarbons and nitrogenous species. The second is the GRI 3.0 mechanism containing 53 species and 325 chemical reactions [39].

4 Comparison of Data and Simulation Results

In Fig. 3, we present experimental and computed values for the flue-gas NO concentration, based on ammonia concentrations in the fuel stream. The experimental values have been corrected for the water removal upstream of the gas analyzers by assuming stoichiometric H_2O production in the flame zone. Error bars in the experimental data represent $\pm 6\sigma$ (σ is the standard deviation). Results from the simulation are shown for three levels of ammonia concentration: 0, 500 ppm, and 1000 ppm NH_3 averaged across the fuel-air mixture. As a convenience for subsequent discussion, Fig. 3 also includes data derived from the reduced model discussed in section 5.2.3, and from simulations incorporating alternative chemistry mechanisms, as discussed in section 5.2.4.

With no ammonia added to the fuel stream, the methane-air nonpremixed flame is found to produce 25 ppm of NO. This level increases to 297 ppm NO in flue gases when the fuel stream contains 1000 ppm NH_3. While the flue gas NO concentration increases with ammonia addition, the conversion rate of NH_3 to NO decreases from over 50% at $[NH_3]_{\text{inlet}} \leq 100$ ppm to less than 30% at $[NH_3]_{\text{inlet}} \geq 800$ ppm. Similar behavior has been observed in previous fuel-nitrogen studies [4].

Generally, the agreement between experiment and model is good at all three ammonia concentrations simulated. The Glarborg *et al.* mechanism overall provides the more accurate and consistent NO predictions. The model results using the GRI 3.0 mechanism overpredict the flue gas NO concentration for the ammonia-enriched flames by as much as 30% in the 1000 ppm case. In Section 5.2.4 we examine the source of these differences.

5 Analysis of Computational Results

5.1 Flame Structure

Based on results from the computational model, the NH_3 content in the fuel stream is found to have no significant effect on the overall flame structure; the results presented in this subsection apply for all methane-air flames investigated. General agreement with previous studies (particularly [14] and others cited below) and the comparison in Section 4 with experimentally-determined flue gas NO concentration provide a measure of model validation. The following discussion is based on the model results using Glarborg *et al.* mechanism.

Two-dimensional temperature and chemical heat release calculated from the model are shown in Fig. 4; advection streamlines are superimposed over the heat release field. Although the computational domain extends to $z = 11$ cm, the image focuses on $0 \leq z \leq 5$ cm. The flame is anchored at an ignition point approximately 0.1

cm above the fuel nozzle. Based on peak temperature, the flame length extends to $z = 3.6$ cm ($T_{\max} = 1847$ K).

The streamlines in Fig. 4b clearly reveal entrainment of oxidizer fluid into the accelerating fuel stream. In the ignition zone ($z \approx 0.1$ cm, $r \approx 0.7$ cm), a rich premixed flame exists on the fuel side, while a lean premixed flame burns on the oxidizer side. A nonpremixed flame is present between the two, located at the ignition zone base. The fuel-rich products from the rich premixed flame mix and burn with the fuel-lean products generated from the lean premixed flame. This structure anchors the flame to its observed position, and has been noted in previous studies [28, 29].

The majority of heat release occurs over an axial span of $0.1 < z < 1.0$ cm, above which a slightly endothermic region is observed on the rich side of the flame zone. The endothermicity is the result of two hydrocarbon dissociation reactions:

$$\begin{aligned} C_2H_5(+M) &\rightleftharpoons C_2H_4 + H(+M)\,, \\ C_2H_3(+M) &\rightleftharpoons C_2H_2 + H(+M)\,. \end{aligned}$$

Endothermicity at the flame tip due to acetylene formation has been observed in the flames simulated by Ern *et al.* [29]. However, the chemical mechanism used in that work did not include ethylene, which is shown to increase the area and magnitude of the endothermic zone in this simulation. The formation of these species has been experimentally confirmed by Gordon *et al.* [40].

The CO and H_2 concentration fields are shown in Fig. 5. In addition to diffusion of CO from off-axis reaction zones, CO is produced within the fuel stream through the hydrocarbon oxidation reactions $HCO + M \rightarrow H + CO + M$. Molecular hydrogen is formed on the rich side of the ignition region primarily through the methane conversion reaction $CH_4 + H \rightarrow CH_3 + H_2$. H_2 diffusing from there into the oxidizer stream is consumed on the lean side of the flame zone in the reaction $OH + H_2 \rightarrow H_2O + H$. The H_2 concentration observed in Fig. 5b is governed primarily by diffusion away from reaction zones at low z and convection towards reaction zones at higher z. As hydrocarbons become scarce at higher axial locations, exothermic CO and H_2 oxidation reactions supply a greater portion of the heat that sustains the flame.

Reaction path analysis reveals the carbon oxidation system shown in Fig. 6. The Appendix descibes how the diagram was generated from the flame simulation. The overall chemical pathways are similar to those observed in premixed flame simulations [41]. Though there is significant chemical activity involving higher hydrocarbons, the bulk of the methane is converted through the $CH_4 \rightarrow CH_3 \rightarrow CH_2O \rightarrow HCO \rightarrow CO \rightarrow CO_2$ path. Generally, the flame chemistry resembles hydrocarbon oxidation on the rich side of the flame zone and CO/H_2 oxidation on the lean side and near the flame tip. The molecular hydrogen produced as a byproduct of hydrocarbon oxidation is primarily converted to H_2O on the lean side of the flame. However, this hydrogen also supplies the bulk of the OH and H radicals through the chain branching reaction $H_2 + O \rightarrow OH + H$.

5.2 Ammonia Oxidation and NO_x Formation

5.2.1 Ammonia-Free Flame

With no ammonia present in the fuel stream, the simulations predict that flue gases from the methane-air flame contain 25 ppm of NO. The mole fraction and chemical production rate of NO for this flame are shown in Fig. 7. The NO_x reaction pathway for the ammonia-free flame is shown in Fig. 8. NO_x formation begins through the prompt-initiating reaction $CH + N_2 \rightarrow HCN + N$ and to a lesser extent through the thermal-NO_x reaction $N_2 + O \rightarrow N + NO$. The sizes of the contributions of these two reactions to the edge $N_2 \rightarrow N$ in Fig. 8 (77% vs 17%) indicates the relative importance of the prompt and thermal mechanisms in this flame; recall that the flame's peak temperature is barely high enough to support thermal NO_x. As can be seen from Fig. 8, the bulk of the nitric oxide is formed from oxidation of atomic nitrogen, with significant contribution from oxidation of HNO and NH. However, most of this N is not formed directly from N_2, but rather is derived from NH that in turn is formed from carbon-bearing species beginning with HCN. The consumption of NO diffusing towards the fuel stream occurs through two reactions:

$$\begin{aligned} NO + HCCO &\rightarrow HCN + CO_2\,, \\ NO + CH_2 &\rightarrow HCN + OH\,. \end{aligned}$$

As discussed in the previous section, hydrocarbons are consumed well below the flame tip, thereby decreasing the activity of the prompt-initiating reaction as axial distance increases. Similar to the H_2 and CO produced at low axial positions as byproducts of hydrocarbon oxidation, the relatively stable HCN produced in the reactions shown above accumulates in the fuel stream and is advected towards the flame tip.

Fig. 7b reveals a two-layer structure in the NO chemistry, which remains nearly parallel to the bulk convection below $z = 3$ cm. Transverse to the flow, nitrogen atoms, bound in the species, NO, HCN, NCO, NH, N and HNO, diffuse back and forth between these two layers. This "recycling" can be observed as the closed loop in Fig. 8. Above $z = 3$ cm, diffusion from the production zone to the consumption layer must compete with the upward fluid advection. The remaining HCN is converted to the more stable NO, which then peaks in concentration along the centerline just above the flame tip. Beyond this location, NO simply diffuses across the domain without further reaction, and is carried out the flue.

Comparison of this mechanism with the prompt mechanism from Miller and Bowman [10] reveals interesting differences. While the initiation reaction is identical, production of NO through the HNO route is absent in Ref. [10]. In the flame studied here, NO recycling through reactions with carbon are minimal. Virtually all of the atomic nitrogen is converted to NO, with negligible N_2 formation. This is likely due to the low NO concentration in this ammonia-free flame, minimizing the effect

of the $N + NO \rightarrow N_2 + O$ reaction. Finally, extensive recycling reactions through cyano-species are captured in the Glarborg *et al.* mechanism. In view of Fig. 8, these reactions play a significant role and lead to a more complex collection of reactions paths than the prompt mechanism shown in Ref. [10].

5.2.2 NO Formation in the Ammonia-Containing Flame

Figure 9 displays a) the NO concentration and b) chemical production rate with 1000 ppm NH_3 added to the fuel stream. Generally, nitrogen species concentrations and chemical production rates increase by an order of magnitude with the addition of 1000 ppm of ammonia to the fuel stream, as does the final flue gas NO concentration (from 25 ppm to 297 ppm). In comparison with Fig. 7a, a dramatically different nitric oxide field is observed in Fig. 9a. The peak in NO concentration has shifted from the area around the flame tip to the ignition region at the flame base. NO formation in the ignition region is an order of magnitude higher than at axial positions $z \geq 1$ cm.

From Figs. 7b and 9b, whether or not ammonia is added, it is clear that net NO production is on the lean side of the flame zone and net NO consumption is on the rich side. Diffusion to the fuel stream causes the NO concentration to reach nearly a third of its peak value along the centerline. Notice that here, the reactions with HCCO and CH_2 are not strong enough to significantly consume the fuel-side NO profile; the pool of hydrocarbons for these reactions has not changed from that of the ammonia-free flame. In Fig. 9a, a mild NO reduction zone is evident in the interior of the flame just below the flame tip from reactions with HCCO.

The reaction pathways that consume ammonia and produce NO and N_2 are shown in Fig. 10. The ammonia is converted to successively smaller amine radicals that are converted to HNO. The bulk of the NO is formed from HNO and atomic nitrogen, with a significant contribution from imidogen (NH).

As seen in the reaction pathway, atomic nitrogen can produce or consume NO. In fuel rich zones, atomic nitrogen consumes NO through the reaction $N+NO \rightarrow N_2+O$, while in fuel lean zones, atomic nitrogen is oxidized to form NO through reactions with OH. In the ignition region, the majority of the atomic nitrogen is oxidized to NO while less than 20% forms N_2, consuming only a fraction of NO in the process. At higher axial positions where NO is more abundant, a greater fraction of the atomic nitrogen converts NO to N_2.

Despite the complexity of the pathway shown in Fig. 10, comparison of the NO formation routes with the ammonia oxidation mechanism shown in Fig. 1 shows excellent agreement. However, the NNH route shown in Fig. 1 is insignificant in this flame.

Comparison of the NO_x formation pathways with and without ammonia present in the fuel stream (Figs. 10 and 8, respectively) reveals some similarities. In both cases, the bulk of the NO is formed either from HNO reactions with H and OH, or

from atomic nitrogen reactions with OH. Both NO formation pathways decrease in NO production as the axial position is increased, though the reason for these changes differs in the two simulations. The NO recycling reactions are identical, and become more dominant at higher axial positions due to the increasing concentration of NO. The prompt-NO_x chemistry of Fig. 8 is also active in the ammonia-containing flame. However, the production of HCN and N from fuel-nitrogen routes in the ignition region are two orders of magnitude higher than from the prompt route, limiting the significance of prompt NO_x chemistry in the ammonia-containing flame.

Finally, the conversion of atomic nitrogen to N_2 through reactions with NO is insignificant in the flame without ammonia, while it is quite significant in the ammonia-containing flame. This is due to the comparatively low nitric oxide concentration in the pure methane-air flame. The activity of the $N + NO \rightarrow N_2 + O$ reaction increases with increasing ammonia concentration resulting in the nonlinear ammonia conversion rate observed in Fig. 3.

5.2.3 Reduced Model Analysis of the Declining Efficiency of NO Production

The results presented both here and in previous studies show that NO production increases with declining efficiency as NH_3 is added to the fuel stream. A reduced model that isolates the conversion of NH_3 to NO can quantify this behavior and help identify the responsible reactions. Note that it does not suffice to effect a reduction of just the chemical mechanism because the conversion of NH_3 to NO depends on the fluid state throughout the flame. Thus the entire chemical-fluid simulation must be reduced, in some way. The following analysis may be useful in elucidating the behavior of trace species in other reacting flows.

Recall that the mass conservation equation for the k-th species is

$$\frac{\partial \rho Y_k}{\partial t} + \nabla \cdot \vec{v} \rho Y_k = \nabla \cdot \rho D_k \nabla Y_k + M_k \dot{\omega}_k$$

in which ρ is the mass density, Y_k is the mass fraction, $\vec{v}$ is the velocity, D_k is a mixture-averaged diffusion coefficient, M_k is the molar mass, and $\dot{\omega}_k$ is the molar rate of formation. The latter is given by [35, Eqs. 48–51]

$$\dot{\omega}_k = \sum_i (\nu_{i,k}^{(r)} - \nu_{i,k}^{(f)}) \left(k_i^{(f)} \prod_\ell C_\ell^{\nu_{i,\ell}^{(f)}} - k_i^{(r)} \prod_\ell C_\ell^{\nu_{i,\ell}^{(r)}} \right)$$

in which k_i is the rate constant of the i-th reaction, $\nu_{i,k}$ is the stoichiometric coefficient of the k-th species in the i-th reaction, C_ℓ is the molar concentration of the ℓ-th species, and the superscripts $^{(f)}$ and $^{(r)}$ indicate forward or reverse.

Suppose the reacting fluid is in steady-state so that the time derivatives vanish, and suppose further the fluid is in a chamber with vanishing composition gradients

normal to any orifices. Then the conservation equations can be integrated over the volume of the chamber to leave

$$\int_{\text{out}} (\vec{n}\cdot\vec{v})\rho Y_k + \int_{\text{in}} (\vec{n}\cdot\vec{v})\rho Y_k = \int_{\text{vol}} M_k \dot{\omega}_k$$

where $\vec{n}$ is the exterior unit normal and the orifices have been segregated into outflow and inflow surfaces. If each species in some group of species is uniformly subject to a multiplicative perturbation, $\pi_k \approx 1$, and if other quantities remain fixed, then the multiplicative perturbations can be pulled outside of the concentrations, densities, and integrals. As a result, the equations above become equations for the scalars π_k.

$$\begin{aligned}
&\left[\int_{\text{out}} (\vec{n}\cdot\vec{v})\rho Y_k\right]\pi_k + \left[\int_{\text{in}} (\vec{n}\cdot\vec{v})\rho Y_k\right]\pi_k = \\
&\quad = \sum_i \left[M_k(\nu_{i,k}^{(r)} - \nu_{i,k}^{(f)}) \int_{\text{vol}} k_i^{(f)} \prod_\ell C_\ell^{\nu_{i,\ell}^{(f)}}\right] \prod_\ell \pi_\ell^{\nu_{i,\ell}^{(f)}} \\
&\qquad - \sum_i \left[M_k(\nu_{i,k}^{(r)} - \nu_{i,k}^{(f)}) \int_{\text{vol}} k_i^{(r)} \prod_\ell C_\ell^{\nu_{i,\ell}^{(r)}}\right] \prod_\ell \pi_\ell^{\nu_{i,\ell}^{(r)}}
\end{aligned} \tag{7}$$

Note that all the quantities in square brackets are fixed and can be determined from the simulation. Upon replacing these quantities by specific numbers, there results a system of algebraic equations that can be solved for the multiplicative perturbations π_k.

In the present situation the species of interest are those except N_2 that contain nitrogen. They are present in such small quantities that fluctuations in them would not be expected to alter the velocity and temperature fields. That is, the rate constants $k_i^{(f)}$ and $k_i^{(r)}$ are insensitive to the nitrogen species, other than N_2, so the model reduction described above applies to them.

To apply the reduced model's equations, (7), we evaluate the quantities in square brackets from the simulation with 1000 ppm of NH_3 flowing in. The equation for ammonia is set aside, and the variable π_{NH_3} is treated as a free parameter. Altogether there are 23 equations and variables for the nitrogen species besides N_2 and NH_3. The equations are solved using Mathematica [42] to express π_k for the remaining nitrogen species as a function of π_{NH_3}. The exact analytic formulas found by Mathematica are too complicated to reproduce here. However, the following low-order Pade approximation for the NO dependent variable is almost indistinguishable from the analytic solution.

$$\pi_{NO} = \frac{2.902\,\pi_{NH_3}^2 + 4.084\,\pi_{NH_3} - 0.017}{\pi_{NH_3}^2 + 4.125\,\pi_{NH_3} + 1.844} \tag{8}$$

It must be emphasized that this reduced model of NO production is specific to the chosen flame configuration. Moreover, far from the validation point, the reduced

model's behavior is at best suggestive. For example, it should not be inferred that equation (8) predicts a ceiling on NO production for large levels of NH_3 seeding because such levels are far in excess of the value at which the reduced model was derived.

The reduced model can be used in a variety of ways to obtain information about the chemical-fluid system. For example, the expression

$$\left[\int_{\text{out}} (\vec{n} \cdot \vec{v}) \rho Y_{\text{NO}}\right] \pi_{\text{NO}}$$

is the reduced model's prediction for the amount of NO flowing out of the reaction chamber. The independent variable, π_{NH_3}, can be similarly scaled to the desired physical units. A graph of this prediction is shown in Fig. 3 along with the experimental data. Note that the reduced model matches the predictions of the reacting flow simulation at 1000 ppm NH_3, as it should, since this is where the reduced model was derived. Moreover, the good agreement with experimental data down past 500 ppm NH_3 is remarkable given the extent of consolidation in creating the reduced model. This indicates that the assumptions of the reduced model remain valid for relatively large changes in NH_3. Near 0 ppm NH_3 the thermal and prompt mechanisms dominate, so the reduced model of NH_3 oxidation fails to predict NO production there.

The reduced model helps identify the reactions responsible for the declining efficiency of NO production. Figure 11 plots the consumption of NO by individual reactions in the Glarborg *et al.* mechanism; information about individual reactions is readily available from the reduced model's formulas. The five reactions that exhibit accelerating consumption with increased seeding are precisely each of those in the mechanism in which NO reacts with another nitrogen species. In order of declining strength they are:

$$\begin{aligned}
\text{N} + \text{NO} &\rightarrow \text{N}_2 + \text{O}, \\
\text{NH} + \text{NO} &\rightarrow \text{N}_2\text{O} + \text{H}, \\
\text{NH} + \text{NO} &\rightarrow \text{N}_2 + \text{OH}, \\
\text{NH}_2 + \text{NO} &\rightarrow \text{N}_2 + \text{H}_2\text{O}, \\
\text{NH}_2 + \text{NO} &\rightarrow \text{NNH} + \text{OH}.
\end{aligned}$$

The first two are by far the strongest of the set. For each reaction, increased NH_3 seeding evidently increases the concentrations of both reactants, and, by the law of mass-action kinetics, has a quadratic effect on the reaction's rate of progress. If the amount consumed by these reactions is added to the net production of NO, then as shown in Fig. 11, the result is a quantity that varies linearly with NH_3 seeding. Thus, these and apparently only these reactions are responsible for the sublinear efficiency of NO production.

5.2.4 Comparison of NO_x Formation Between Mechanisms

Reaction pathway analysis of simulations using the GRI 3.0 mechanism provide similar results to those shown in Figs. 8 and 10 for the Glarborg *et al.* mechanism, though some significant differences are evident. The key difference between mechanisms is the level of conversion of NH to HNO. In the Glarborg *et al.* mechanism, this occurs through reaction with hydroxyl radical, with about 20% of the NH being converted to HNO. Using GRI 3.0, two additional NH → HNO conversion routes exist:

$$\mathrm{NH + H_2O \leftrightarrow HNO + H_2} \qquad k = 2 \cdot 10^{13} \exp\left(-\tfrac{13850}{RT}\right) \qquad \text{Rx. 195}$$

$$\mathrm{NH + CO_2 \leftrightarrow HNO + CO} \qquad k = 1 \cdot 10^{13} \exp\left(-\tfrac{14350}{RT}\right) \qquad \text{Rx. 278}$$

Reaction numbers are given in the order listed in the GRI 3.0 mechanism. These two additional reactions increase the NH → HNO conversion by a factor of two, which comes at the cost of the NH → N conversion. For both mechanisms, virtually all HNO is converted to NO, while atomic nitrogen may produce or consume NO depending upon local combustion conditions. This favoring of HNO over N leads to the higher NO concentrations predicted by the GRI 3.0 mechanism.

The validity of the rate expressions for the two reactions, above, has been called into question in previous studies [43]. To assess the claims suggested in the reference, three simulations were performed using the GRI 3.0 mechanism with reactions 195 and 278 removed; results are included in Fig. 3 as the modified GRI mechanism. With 1000 ppm of ammonia in the fuel stream, the agreement between simulation and experiment improves significantly. This dramatic effect is not observed in the ammonia-free flame; the removal leads to a slight increase (5 ppm) in flue gas NO concentration. In the ammonia-free flames, nearly all atomic nitrogen and nitroxyl are oxidized to NO (Fig. 8) so that conversion of NH to either species in ammonia-free flames yields the same NO production.

Further comparison of mechanisms using the PREMIX flame code [44] reveals that the removal of these reactions results in only a 3% decrease in NO concentration. This implies that the strong effect of these reactions may be limited to nonpremixed flames.

6 Conclusions

In this study, the conversion of volatile fuel-nitrogen species is investigated through a series of experiments and computations involving a laminar coflowing nonpremixed flame. In one series of experiments, increasing concentrations of ammonia are added to the fuel stream of a methane-air flame. The conversion of ammonia to nitric oxide is found to decrease from over 50% at low ammonia concentration to less than 30% at higher ammonia concentration. These experiments are compared with simulations

results at three different ammonia concentration using two different chemical mechanisms. Better agreement between experiment and model is found using the Glarborg *et al.* mechanism.

A two-zone NO_x formation structure is observed in the ammonia-free flame. At low axial positions, NO_x formation closely follows the prompt mechanism, with significant production through the HNO intermediate. The thermal mechanism is insignificant due to the low temperatures (1800 K) found in this flame. Significant NO consumption occurs on the fuel side of the flame through reactions with hydrocarbon radicals. The resulting HCN is advected upward along the axis, and converted back to NO as it crosses at the flame tip. In the ammonia-seeded case, much more NO is produced than can be consumed by the available CH_2 and HCCO. Moreover, for the larger ammonia seeding rates, a greater fraction of the NO produced is converted to N_2.

Simulations using both the Glarborg *et al.* and the GRI 3.0 chemical mechanisms match experimental flue gas measurements quite well. The Glarborg *et al.* mechanism produces more accurate and consistent results; its performance is attributed to the differences in the HNO-formation reactions and the more complete NO-recycling chemistry.

A Appendix. Reaction Path Diagrams

The reaction path diagrams appearing in this paper are generated from the flame simulations. Automatically generated reaction path diagrams have appeared elsewhere. For example, Warnatz *et al.* [45] discuss "integral reaction flow analysis" with edge weights integrated over a region of space, as in this paper, or over an interval of time. We wish to acknowledge the help of Prof. D. G. Goodwin in formulating an approach based on conserved scalars.

Only conserved scalars provide a consistent measure of the exchange of material among species due to chemical reactions. Thus, for species s_1 and s_2, let $n_i(s_1, s_2) \geq 0$ be the rate (mol/cm^3 s) at which a chosen element's atoms are transferred from s_1 to s_2 as a result of reaction i. The total transfer of the element from s_1 to s_2 is then $\sum_i \int_{\text{vol}} n_i(s_1, s_2)$ (mol/s), where the sum is over all reactions and the integral is over the domain of the flame simulation. This quantity is the weight of the path $s_1 \rightarrow s_2$ in the reaction path diagram. The data needed to evaluate these weights is readily available from the simulation and from CHEMKIN.

A minor difficulty arises because the CHEMKIN description of chemical reactions is inadequate to infer $n_i(s_1, s_2)$ in all cases. For example, whether the reaction i : $\mathrm{OH} + \mathrm{H_2} \rightarrow \mathrm{H_2O} + \mathrm{H}$ shifts an O or an H atom between the reactants affects to which product species the reactant hydrogen atoms are transferred. The few ambiguous cases that occur in the CHEMKIN mechanisms are resolved by supposing that the reaction shifts the species fragment of lower molecular weight.

References

[1] C. T. Bowman. Control of combustion-generated nitrogen oxide emissions: technology driven by regulation. *Proc. Comb. Inst.*, 24:859–878, 1992.

[2] S. R. Turns. Understanding NO_x formation in nonpremixed flames: experiments and modeling. *Prog. Energy Combust. Sci.*, 21:361–385, 1995.

[3] C. P. Fenimore. Formation of nitric oxide from fuel nitrogen in ethylene flames. *Combust. Flame*, 19:289–296, 1972.

[4] A. F. Sarofim, G. C. Williams, M. Modell, and S. M. Slater. Conversion of fuel nitrogen to nitric oxide in premixed and diffusion flames. *AIChE Symp. Ser.*, 71(148):51–61, 1975.

[5] V. A. Krutiev and A. D. Gorbanenko. *Teploenergetika*, 23(10):72–74, 1976. In Russian.

[6] H. Sarv and N. P. Cernansky. NO_x formation from the combustion of monodisperse n-heptane sprays doped with fuel-nitrogen additives. *Combust. Flame*, 76:265–283, 1989.

[7] J. P. Hämäläinen and M. J. Aho. Effect of fuel composition on the conversion of volatile solid fuel-N to N_2O and NO. *Fuel*, 74(12):1922–1924, 1995.

[8] J. B. Mereb and J. O. L. Wendt. Air staging and reburning mechanisms for NO_x abatement in a laboratory coal combustor. *Fuel*, 73(7):1020–1026, 1994.

[9] J. Zhou, S. M. Masutani, D. M. Ishimura, S. Q. Turn, and C. M. Kinoshita. Release of fuel-bound nitrogen during biomass gasification. *Ind. Eng. Chem. Res.*, 39:626–634, 2000.

[10] J. A. Miller and C. T. Bowman. Mechanism and modeling of nitrogen chemistry in combustion. *Prog. Energy Combust. Sci.*, 15(4):287–338, 1989.

[11] J. A. Miller, M. D. Smooke, R. M. Green, and R. J. Kee. Kinetic modeling of the oxidation of ammonia in flames. *Combust. Sci. Tech.*, 34:149–176, 1983.

[12] E. G. Eddings, P. J. Smith, M. P. Heap, D. W. Pershing, and A. F. Sarofim. The use of models to predict the effect of fuel switch on NO_x emissions. In R. W. Bryers and N. S. Harding, editors, *Coal-Blending and Switching of Low-Sulfur Western Coals*, pages 169–184. ASME for The Engineering Foundation, 1994. Papers presented at The Engineering Foundation Conference on Coal-Blending and Switching of Low-Sulfur Western Coals, Snowbird, Utah, September 26–October 1, 1993.

[13] K. C. Smyth. NO production and destruction in a methane/air diffusion flame. *Combust. Sci. Tech.*, 115:151–176, 1996.

[14] M. D. Smooke, A. Ern, M. A. Tanoff, B. A. Valdati, R. K. Mohammed, D. F. Marran, and M. B. Long. Computational and experimental study of NO in an axisymmetric laminar diffusion flame. *Proc. Comb. Inst.*, 26:2161–2170, 1996.

[15] M. C. Drake and R. J. Blint. Thermal NO_x in stretched laminar opposed-flow diffusion flames with $CO/H_2/N_2$ fuel. *Combust. Flame*, 76:151–167, 1989.

[16] M. C. Drake and R. J. Blint. Relative importance of nitric oxide formation mechanisms in laminar opposed-flow diffusion flames. *Combust. Flame*, 83:185–203, 1991.

[17] S. P. Burke and T. E. W. Schumann. Diffusion flames. *Ind. Engin. Chem.*, 20(10):998, 1928.

[18] F. G. Roper. The prediction of laminar jet diffusion flame sizes: Part I. theoretical model. *Combust. Flame*, 29:219–226, 1977.

[19] F. G. Roper, C. Smith, and A. C. Cunningham. The prediction of laminar jet diffusion flame sizes: Part II. experimental verification. *Combust. Flame*, 29:227–234, 1977.

[20] A. S. Gordon, S. C. Li, P. A. Libby, and F. A. Williams. Influence of initial velocity distributions on the height of methane-air nonpremixed flames. *Combust. Sci. Tech.*, 100:395–399, 1994.

[21] A. S. Gordon, S. C. Li, and F. A. Williams. Visible flame heights of laminar coflow diffusion flames. *Combust. Sci. Tech.*, 141:1–18, 1999.

[22] J. A. Miller and R. J. Kee. Chemical nonequilibrium effects in hydrogen-air laminar jet diffusion flames. *J. Phys. Chem.*, 81(25):2534–2541, 1977.

[23] S. H. Chung and C. K. Law. Burke-Schumann flame with streamwise and preferential diffusion. *Combust. Sci. Tech.*, 37:21–46, 1984.

[24] S. Ishizuka and Y. Sakai. Structure and tip-opening of laminar diffusion flames. *Proc. Comb. Inst.*, 21:1821–1828, 1986.

[25] T. Takagi and Z. Xu. Numerical analysis of laminar diffusion flames — effects of preferential diffusion of heat and species. *Combust. Flame*, 96:50–59, 1994.

[26] M. D. Smooke, R. E. Mitchell, and D. E. Keyes. Numerical solution of two-dimensional axisymmetric laminar diffusion flames. *Combust. Sci. Tech.*, 67:85, 1989.

[27] M. D. Smooke, P. Lin, J. K. Lam, and M. B. Long. Computational and experimental study of a laminar axisymmetric methane-air diffusion flame. *Proc. Comb. Inst.*, 23:575–582, 1990.

[28] Y. Xu, M. D. Smooke, P. Lin, and M. B. Long. Primitive variable modeling of multidimensional laminar flames. *Combust. Sci. Tech.*, 90:289, 1993.

[29] A. Ern, C. C. Douglas, and M. D. Smooke. Detailed chemistry modeling of laminar diffusion flames on parallel computers. *Int. J. Sup. App.*, 9:167–186, 1995.

[30] M. D. Smooke, C. S. McEnally, L. D. Pfefferle, R. J. Hall, and M. B. Colket. Computational and experimental study of soot formation in a coflow, laminar diffusion flame. *Combust. Flame*, 117:117–139, 1999.

[31] C. S. McEnally, L. D. Pfefferle, A. M. Schaffer, M. B. Long, R. K. Mohammed, M. D. Smooke, and M. B. Colket. Characterization of a coflowing methane/air non-premixed flame with computer modelling, Rayleigh-Raman imaging, and on-line mass spectrometry. *Proc. Comb. Inst.*, 28:2063–2070, 2000.

[32] M. Nishioka, Y. Takemoto, H. Yamashita, and T. Takeno. Effects of multi-dimensionality on a diffusion flame. *Proc. Comb. Inst.*, 26:1071–1077, 1996.

[33] X. L. Zhu, M. Nishioka, and T. Takeno. NO emission characteristics of methane-air coflow partially premixed flame. *Proc. Comb. Inst.*, 27:1369–1376, 1998.

[34] M. S. Day and J. B. Bell. Numerical simulation of laminar reacting flows with complex chemistry. *Combust. Theory Modelling*, 4:535–556, 2000.

[35] R. J. Kee, R. M. Ruply, E. Meeks, and J. A. Miller. Chemkin-III: A FORTRAN chemical kinetics package for the analysis of gas-phase chemical and plasma kinetics. Technical Report SAND96-8216, Sandia National Laboratories, 1996.

[36] R. S. Barlow. Turbulent nonpremixed flame workshop. http://www.ca.sandia.gov/tdf/Workshop/Submodels.html.

[37] R. J. Kee, G. Dixon-Lewis, J. Warnatz, M. E. Coltrin, and J. A. Miller. A FORTRAN computer code package for the evaluation of gas-phase multicomponent transport properties. Technical Report SAND86-8246, Sandia National Laboratories, 1986.

[38] P. Glarborg, M. U. Alzueta, K. Dam-Johansen, and J. A. Miller. Kinetic modelling of hydrocarbon/nitric oxide interactions in a flow reactor. *Combust. Flame*, 115:1–27, 1998.

[39] G. P. Smith, D. M. Golden, M. Frenklach, N. W. Moriarty, B. Eiteneer, M. Goldenberg, C. T. Bowman, R. K. Hanson, S. Song, W. C. Gardiner Jr., V. V. Lissianski, and Z. Qin. GRI-Mech home page. http://www.me.berkeley.edu/gri_mech/.

[40] A. S. Gordon, S. R. Smith, and J. R. McNesby. *Proc. Comb. Inst.*, 7:317, 1958.

[41] J. Warnatz. Rate coefficients in the C/H/O system. In W. C. Gardiner Jr., editor, *Combustion Chemistry*, pages 197–360. Springer-Verlag, New York, 1984.

[42] S. Wolfram. *The Mathematica Book*. Wolfram Media / Cambridge University Press, Champaign, Illinois and Cambridge, United Kingdom, fourth edition, 1999.

[43] P. Glarborg, P. G. Kristensen, K. Dam-Johansen, M. U. Alzueta, A. Millera, and R. Bilbao. Nitric oxide reduction by non-hydrocarbon fuels. Implications for reburning with gasification gases. *Energy Fuels*, 14:828–838, 2000.

[44] R. J. Kee, J. F. Grcar, M. D. Smooke, and J. A. Miller. A fortran program for modeling steady, laminar, one-dimensional premixed flames. Technical Report SAND85-8240, Sandia National Laboratories, 1983.

[45] J. Warnatz, U. Mass, and R. W. Dibble. *Combustion*. Springer-Verlag, Berlin, 3rd edition, 2001.

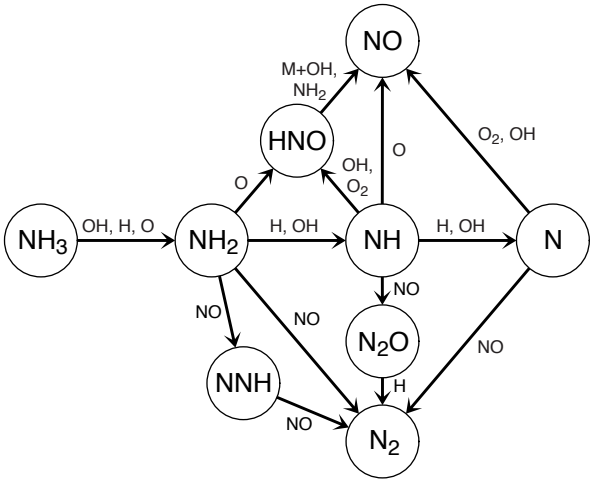

Figure 1: *Ammonia oxidation mechanism [11].*

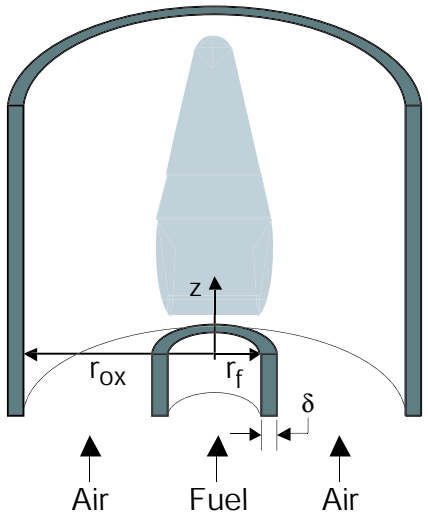

Figure 2: *Schematic of laminar, coflowing, nonpremixed flame.*

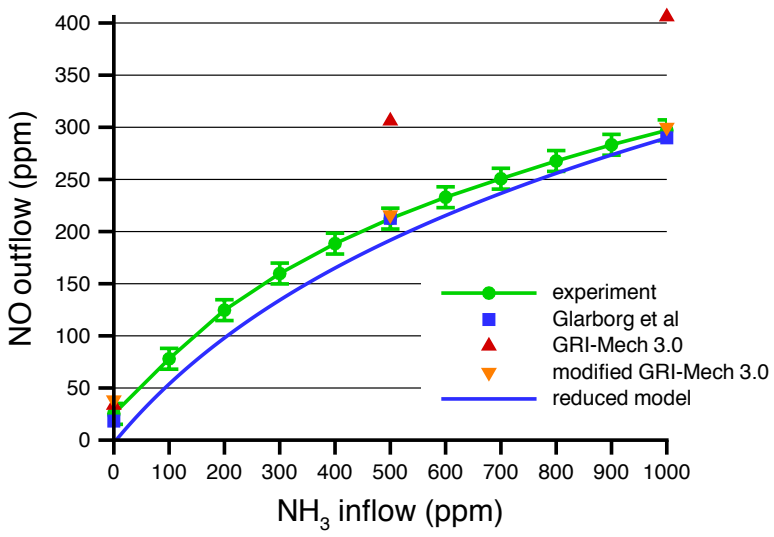

Figure 3: *Measured and computed flue-gas NO concentrations versus NH_3 seeding as a fraction of the total fuel-air inflow (ammonia is added only to the fuel stream). Error bars on the experimental data represent $\pm 6\sigma$. The reduced-model curve is discussed in section 5.2.3, and the GRI data is discussed in section 5.2.4.*

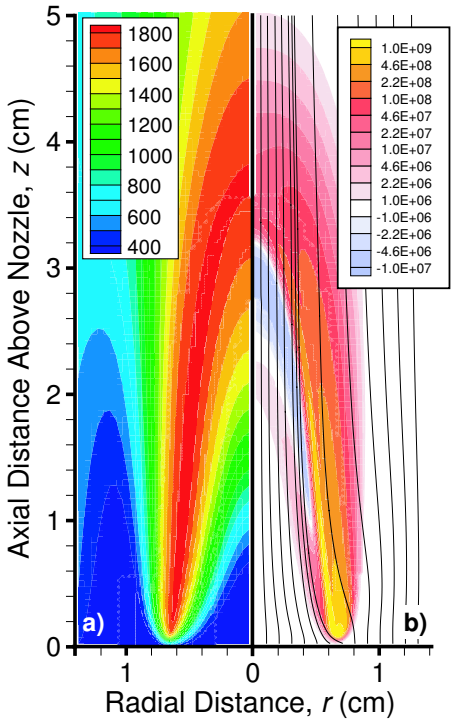

Figure 4: *a) Temperature (K) and b) chemical heat release (ergs/cm^3 s) with superimposed advection streamlines. Note: a nonlinear scale for the heat release contours is used to highlight the triple flame structure.*

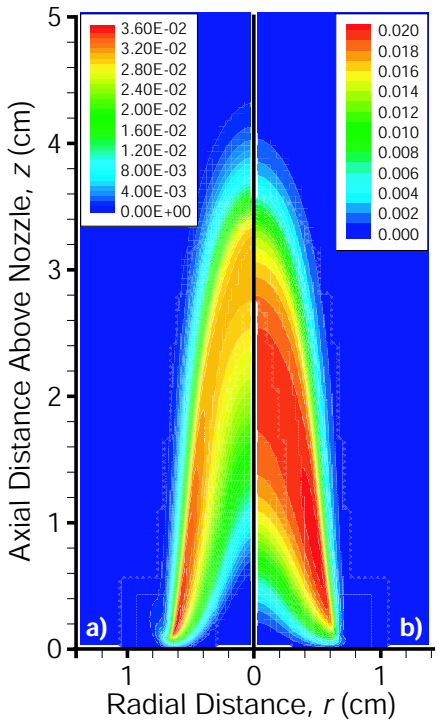

Figure 5: *Mole fractions of a) carbon monoxide and b) molecular hydrogen.*

(100) $\mathbf{CH_4 \rightarrow CH_3}$
68% +H
26% +OH
(77) $\mathbf{CO \rightarrow CO_2}$
98% +OH
(50) $\mathbf{HCO \rightarrow CO}$
78% +M
(47) $\mathbf{CH_2O \rightarrow HCO}$
52% +OH
34% +H
10% $+CH_3$
(33) $\mathbf{C_2H_4 \rightarrow C_2H_3}$
80% +H
19% +OH
(29) $\mathbf{C_2H_3 \rightarrow C_2H_2}$
65% +M
15% +H
13% $+CH_3$

(28) $\mathbf{C_2H_5 \rightarrow C_2H_4}$
99% +M
(20) $\mathbf{CH_2OH \rightarrow CH_2O}$
83% +M
13% $+O_2$
(20) $\mathbf{CH_3 \rightarrow CH_4}$
53% +H+M
23% $+CH_2O$
(18) $\mathbf{CH_3 \rightarrow CH_2OH}$
100% +OH
(17) $\mathbf{C_2H_2 \rightarrow HCCO}$
100% +O

(16) $\mathbf{CH_3 \rightarrow CH_2O}$
98% +O
(15) $\mathbf{CH_3 \rightarrow C_2H_6}$
100% $+CH_3$
(15) $\mathbf{C_2H_6 \rightarrow C_2H_5}$
64% +H
20% +OH
11% $+CH_3$
(13) $\mathbf{CH_3 \rightarrow C_2H_5}$
100% $+CH_3$
(9) $\mathbf{HCCO \rightarrow CO}$
57% +H
26% $+O_2$

(8) $\mathbf{CH_2(S) \rightarrow CH_2}$
60% $+N_2$
29% $+H_2O$
(7) $\mathbf{CH_3 \rightarrow CH_2(S)}$
79% +OH
20% +H
(5) $\mathbf{HCCO \rightarrow CH_2(S)}$
100% +H
(5) $\mathbf{HCCO \rightarrow C_2O}$
100% +OH
(4) $\mathbf{CH_2 \rightarrow C_2H_4}$
100% $+CH_3$

(4) $\mathbf{CH_2 \rightarrow CH_2O}$
74% +OH
24% $+CO_2$
(4) $\mathbf{C_2O \rightarrow CO}$
58% $+O_2$
26% +OH
(4) $\mathbf{CH_3 \rightarrow C_2H_4}$
98% $+CH_2$
(4) $\mathbf{CO_2 \rightarrow CO}$
32% +H
31% $+CH_2(S)$
25% $+CH_2$

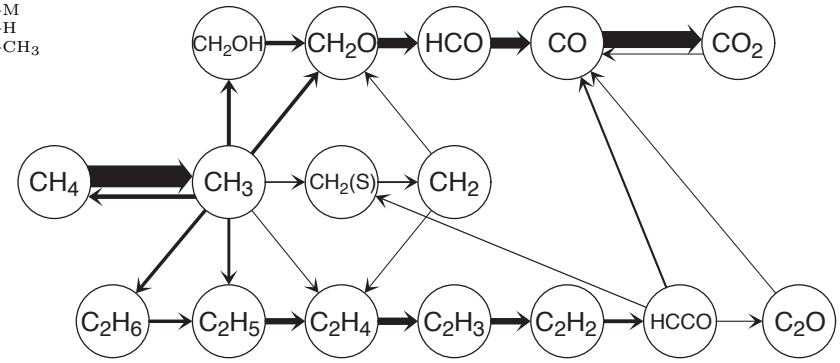

Figure 6: *Carbon reaction paths (Glarborg et al. mechanism). The thickness of an arrow indicates the quantity (mol/s) of atomic carbon moving through the path; only paths at least 4% of the greatest are shown. The table notes the percent of each path due to various reactions; only contributions of at least 10% are listed.*

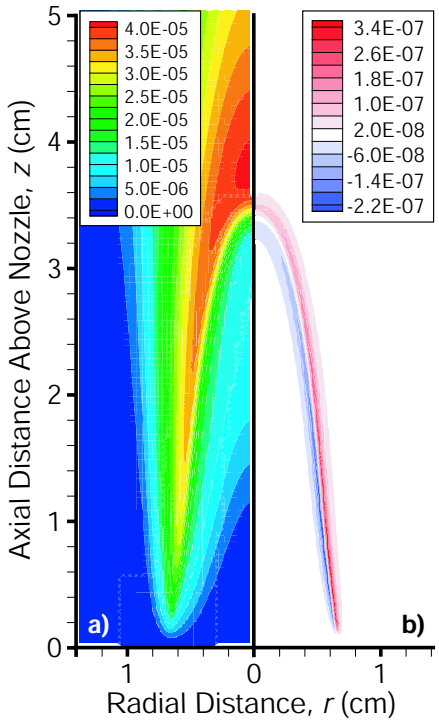

Figure 7: *Nitric oxide a) mole fraction and b) net production rate (mole/cm^3 sec) for the ammonia-free methane-air flame.*

(100) $\mathbf{N_2 \rightarrow NNH}$
51% +H+O_2
48% +H
(96) $\mathbf{NNH \rightarrow N_2}$
91% +O_2
(26) $\mathbf{NO_2 \rightarrow NO}$
77% +H
18% +O
(24) $\mathbf{NO \rightarrow NO_2}$
66% +O+M
33% +HO_2
(15) $\mathbf{HNO \rightarrow NO}$
49% +H
45% +OH
(14) $\mathbf{N_2 \rightarrow N_2O}$
100% +O+M
(14) $\mathbf{N_2O \rightarrow N_2}$
96% +H
(12) $\mathbf{NO \rightarrow HNO}$
80% +H+M
11% +H+N_2

(9) $\mathbf{N \rightarrow NO}$
80% +OH
11% +O_2

(8) $\mathbf{NO \rightarrow HCN}$
57% +HCCO
22% +CH_2
(6) $\mathbf{NH \rightarrow N}$
68% +H
32% +OH
(5) $\mathbf{NCO \rightarrow NH}$
100% +H
(5) $\mathbf{HCN \rightarrow NCO}$
100% +O
(4) $\mathbf{HNCO \rightarrow NH_2}$
100% +H
(3) $\mathbf{NH_2 \rightarrow NH}$
55% +H
40% +OH
(3) $\mathbf{NCO \rightarrow HNCO}$
70% +H_2O
21% +H_2
(3) $\mathbf{CN \rightarrow NCO}$
66% +OH
31% +O_2
(3) $\mathbf{NO \rightarrow HCNO}$
68% +CO
32% +H

(3) $\mathbf{NH \rightarrow HNO}$
96% +OH
(2) $\mathbf{NH \rightarrow NO}$
98% +O
(2) $\mathbf{HCN \rightarrow CN}$
49% +H
44% +OH
(2) $\mathbf{HCNO \rightarrow NO}$
79% +OH
21% +H
(2) $\mathbf{HOCN \rightarrow NCO}$
96% +H
(2) $\mathbf{NO \rightarrow HONO}$
100% +OH+M

(2) $\mathbf{HONO \rightarrow NO_2}$
91% +OH
(2) $\mathbf{N_2 \rightarrow N}$
77% +CH
17% +O
(2) $\mathbf{HCN \rightarrow HOCN}$
100% +OH
(2) $\mathbf{H_2CN \rightarrow HCN}$
100% +M
(2) $\mathbf{N_2 \rightarrow HCN}$
100% +CH
(1) $\mathbf{N \rightarrow H_2CN}$
100% +CH_3
(1) $\mathbf{NNH \rightarrow N_2O}$
100% +O
(1) $\mathbf{NCO \rightarrow NO}$
99% +O
(1) $\mathbf{N_2O \rightarrow NO}$
76% +H
23% +O
(1) $\mathbf{HCN \rightarrow NH}$
100% +O

(1) $\mathbf{CH_2CN \rightarrow CN}$
98% +O
(1) $\mathbf{HCN \rightarrow CH_3CN}$
100% +CH_3
(1) $\mathbf{CH_3CN \rightarrow CH_2CN}$
87% +H
12% +OH
(1) $\mathbf{N_2O \rightarrow NH}$
99% +H
(1) $\mathbf{CN \rightarrow HCN}$
39% +CH_4
33% +C_2H_4
(0.9) $\mathbf{NO \rightarrow N}$
61% +C
38% +CH
(0.8) $\mathbf{NO \rightarrow CN}$
55% +C_2H
44% +C
(0.8) $\mathbf{NH_2 \rightarrow NH_3}$
42% +H+M
41% +H_2O
15% +H_2

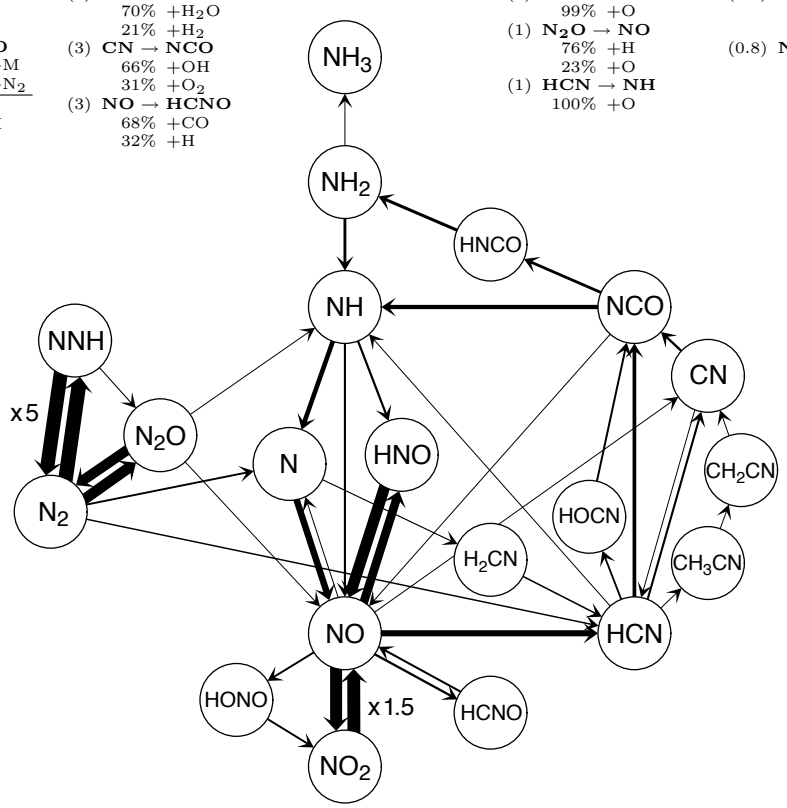

Figure 8: *Nitrogen reaction paths for the flame without ammonia seeding (Glarborg et al. mechanism). Note the continuous recycling of nitrogen: starting in the form of NO, it passes through carbon-bearing species to NH and finally back to NO. The thickness of an arrow indicates the quantity (mol/s) of atomic nitrogen moving through the path; only paths at least* 0.8% *of the greatest are shown. The table notes the percent of each path due to various reactions; only contributions of at least 10% are listed. The strongest paths (above the line in the table) are reversible and net to weaker paths.*

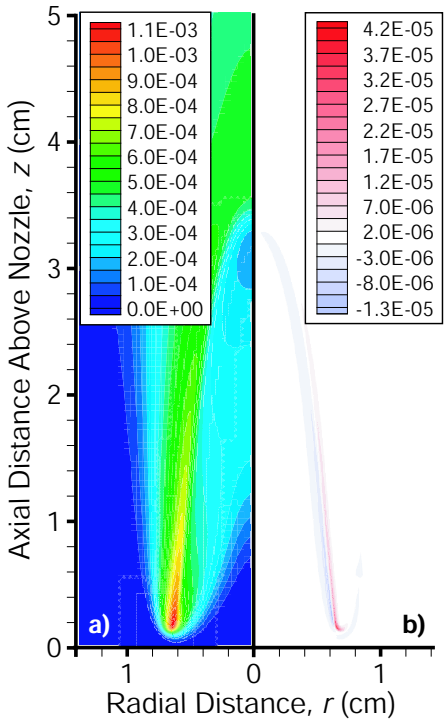

Figure 9: *Nitric oxide a) mole fraction and b) net production rate (mole/cm^3 sec) for the simulation with 1000 ppm ammonia in the fuel stream.*

(100) **$NO_2 \rightarrow NO$**
79% +H
15% +O
(89) **$NO \rightarrow NO_2$**
63% +M
36% +OH

(74) **$NH_3 \rightarrow NH_2$**
65% +OH
28% +H
(72) **$NH_2 \rightarrow NH$**
60% +H
35% +OH
(70) **HNO → NO**
49% +H
39% +OH
(48) **NH → N**
72% +H
27% +OH
(40) **NO → HNO**
74% +H+M
11% +H+N_2
10% +HCO

(33) **N → NO**
78% +OH
13% +O_2
(32) **NO → HCN**
51% +HCCO
26% +CH_2
(21) **NH → HNO**
94% +OH
(20) **NCO → NH**
100% +H
(20) **NNH → N2**
71% +O_2
18% +
(18) **HCN → NCO**
100% +O
(17) **NO → N_2**
58% +N
23% +NH_2
16% +NH
(16) **NH → NO**
96% +O

(16) **$N_2O \rightarrow N_2$**
86% +H
10% +M
(14) **HNCO → NH_2**
100% +H
(13) **NCO → HNCO**
68% +H_2O
19% +H_2
(12) **$N_2 \rightarrow NNH$**
53% +H+O_2
46% +H
(12) **$H_2CN \rightarrow HCN$**
100% +M

(12) **NO → HCNO**
61% +CO
38% +H
(11) **CN → NCO**
61% +OH
36% +O_2
(11) **NO → HONO**
100% +OH+M
(11) **HONO → NO_2**
89% +OH
(11) **HCNO → NO**
74% +OH
25% +O
(10) **HCN → CN**
48% +H
44% +OH
(10) **N → N_2**
96% +NO
(10) **NO → N_2O**
97% +NH

(10) **NH → N_2O**
99% +NO
(9) **N → H_2CN**
100% +CH_3
(9) **HOCN → NCO**
96% +H
(8) **HCN → HOCN**
100% +OH
(7) **NH_2 → HNO**
100% +O
(5) **NCO → NO**
99% +O
(5) **CH_2CN → CN**
99% +O
(5) **HCN → CH_3CN**
100% +CH_3
(4) **HCN → NH**
100% +O
(4) **CH_3CN → CH_2CN**
86% +H
13% +OH
(4) **NH_2 → N_2**
93% +NO

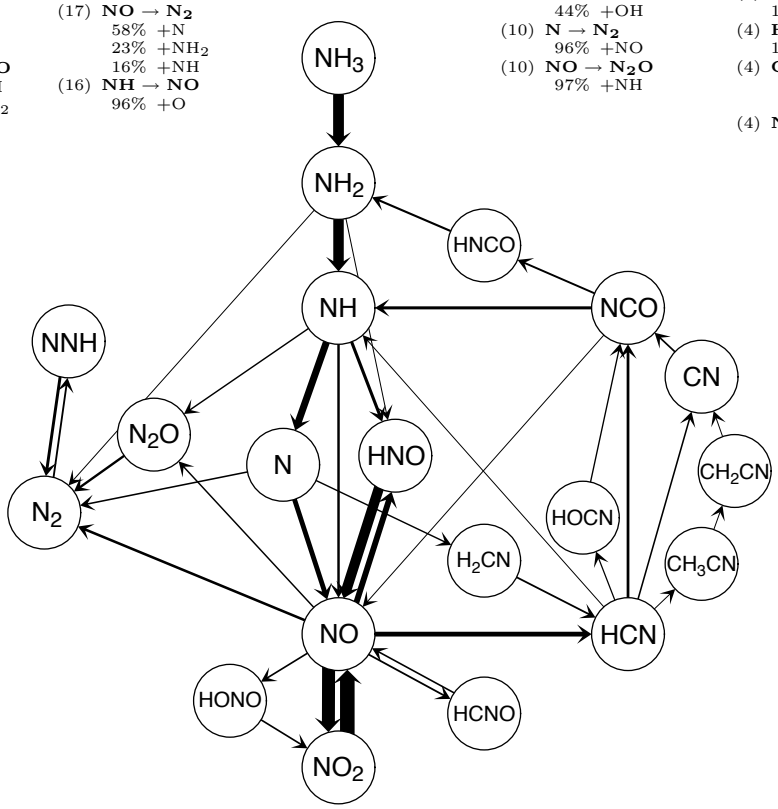

Figure 10: *Nitrogen reaction paths for the ammonia-seeded flame (Glarborg et al. mechanism). The thickness of an arrow indicates the quantity (mol/s) of atomic nitrogen moving through the path; only paths at least 4% of the greatest are shown. The table notes the percent of each path due to various reactions; only contributions of at least 10% are listed. The strongest paths (above the line in the table) are opposed and net to a weaker path.*

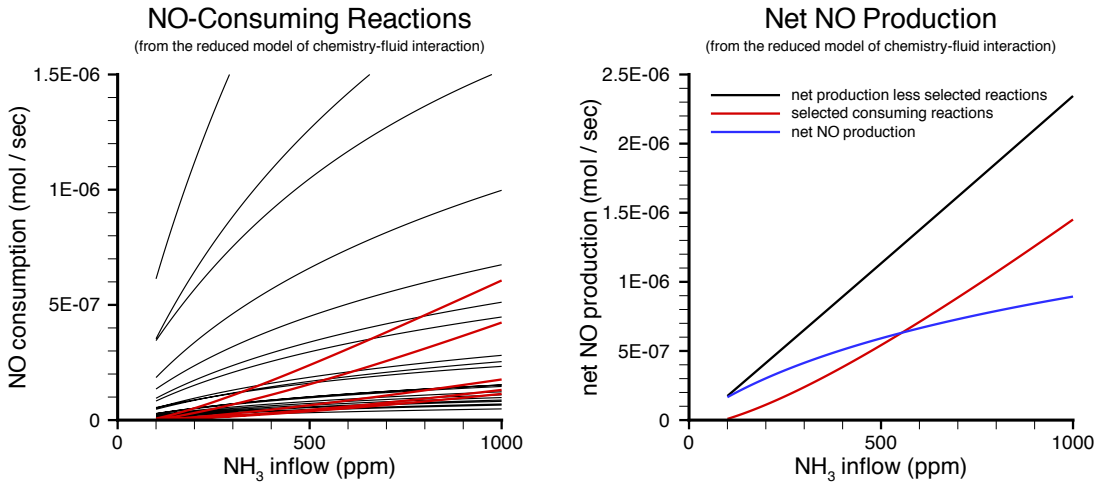

Figure 11: *(Left) The reduced model's predictions of NO consumption by reactions in the Glarborg et al. mechanism. Five reactions (red) accelerate their consumption of NO with increased ammonia seeding. (Right) When the amount of NO consumed by these reactions is restored to the net NO production, the total has a linear variation with the amount of* NH_3 *seeding.*